Constraints on core-mantle boundary topography from normal mode splitting

Gaia Soldati,[1] Paula Koelemeijer,[2] Lapo Boschi,[3] Arwen Deuss[2]

[1]Istituto Nazionale di Geofisica e Vulcanologia, Roma, Italy.

(gaia.soldati@ingv.it)

[2]Department of Earth Sciences, University of Cambridge, Cambridge, UK

[3]Institute de Sciences de le Terre de Paris, Université Pierre et Marie Curie, Paris, France.

This article has been accepted for publication and undergone full peer review but has not been through the copyediting, typesetting, pagination and proofreading process, which may lead to differences between this version and the Version of Record. Please cite this article as doi: 10.1002/ggge.20115

Abstract. The frequencies of Earth's normal modes are split by rotation, ellipticity, and internal structure of the Earth. Thus, models of mantle heterogeneity and discontinuity topography generate splitting that may be tested against observations. We insert maps of core-mantle boundary (CMB) topography, which are derived via either a purely seismic or a joint tomographic/geodynamic inversion of body waves data, on top of tomographic model S20RTS. We then calculate synthetic splitting functions for normal modes that have been shown to be sensitive to CMB topography and compare these to observed normal mode splitting data. The CMB topography maps obtained via geodynamically-constrained tomography fit normal mode data better than purely seismic maps, in particular when the geodynamic constraint also accounts for the presence of post-perovskite in the D" region. We test the significance of the reduction in misfit using the concept of observability which suggests that normal modes are able to observe the difference between the different CMB topography maps. In addition, we find that the statistical significance, assessed by checking what fraction of 1000 randomly generated CMB models achieve a comparatively good fit as the desired model, is higher than 92 % for degree 2 and 98 % for all degrees. In summary, we have identified a model of CMB topography that fits body wave data and improves, at least to some extent, the fit to normal mode data, and is coherent with the large-scale pattern of deep mantle heterogeneity expected on the basis of convection modelling.

1. Introduction

The core-mantle boundary (CMB) has a key role in the dynamics of deep mantle convection, the geodynamo and the evolution of the core, and has therefore been intensively studied from the beginning of the 1980's. Maps of CMB topography have been derived on the basis of seismological inversions of body wave travel-times [e.g. *Morelli and Dziewonski*, 1987; *Rodgers and Wahr*, 1993; *Obayashi and Fukao*, 1997; *Boschi and Dziewonski*, 2000; *Soldati et al.*, 2003] or normal-mode splitting [*Li et al.*, 1991b; *Ishii and Tromp*, 1999]. Alternatively, they are derived through a geodynamic approach [*Forte et al.*, 1995; *Lassak et al.*, 2007, 2010] which assumes that the CMB should be depressed/uplifted under relatively dense/light regions of the lowermost mantle. Despite the general agreement on the overall shape of CMB undulations (depression under the circum-Pacific Ring and elevation below the Central Pacific), the details of the peak-to-peak amplitude and pattern are still debated.

Soldati et al. [2012] proposed a joint seismic-geodynamic technique to invert body wave data taking into account the coupling of CMB topography with mantle heterogeneity by viscous flow. The P-wave velocity models of the mantle they obtained this way fit body wave data as well as the purely seismically derived ones and the corresponding maps of CMB topography are more stable (i.e. no observed discrepancy between maps based on PcP-PKP datasets) and have lower amplitude. In this formulation, the response of CMB topography to mantle density perturbations depends on the radial viscosity profile of the mantle. The perovskite to post-perovskite phase change in the D" region [*Murakami et al.*, 2004; *Oganov and Ono*, 2004] may be modelled as a reduction in mantle viscosity of three

orders of magnitude [*Yamazaki et al.*, 2006; *Ammann et al.*, 2010; *Cizkova et al.*, 2010]. The ellipticity of the resulting CMB maps can match the very-long baseline interferometry (VLBI) data [*Gwinn et al.*, 1986] only when the post-perovskite related low viscosity jump is included. This partially confirms the findings by *Nakagawa and Tackley* [2005] that geodynamic models with a low-viscosity post-perovskite layer can include high-density piles without producing unacceptably large CMB topography, and the analysis by *Mosca et al.* [2012], whose probabilistic approach to joint body wave, surface wave, and normal mode tomography favor deep mantle chemical heterogeneity (including post-perovskite).

Earth's normal modes have a completely different sensitivity than body waves to the lateral structure of both the mantle and CMB due to their global character. Normal-mode based CMB topography maps published so far [*Li et al.*, 1991b; *Ishii and Tromp*, 1999] are poorly correlated with the results of body wave travel-time imaging [*Morelli and Dziewonski*, 1987; *Sze and van der Hilst*, 2003; *Soldati et al.*, 2012]. In this contribution, we make use of existing normal mode data to investigate the influence of the different CMB topography maps of *Soldati et al.* [2012] (Figure 1) and the effect of a low viscosity post-perovskite layer on the splitting of Earth's free oscillations.

2. Theory and Data

The occurrence of large earthquakes makes the Earth ring at discrete frequencies as first observed following the Chile earthquake of 1960 [*Benioff et al.*, 1961]. Spheroidal modes ${}_nS_l$ and toroidal modes ${}_nT_l$ are characterised by their radial order n and angular order l, consisting of $2l+1$ singlets with azimuthal order m. Modes are degenerate (i.e. all $2l+1$ singlets have the same frequency) for a spherically symmetric, isotropic, non-rotating Earth model. In a more realistic Earth (e.g. aspherical) the effects of Earth's

rotation, ellipticity and lateral heterogeneity, including discontinuity topography, remove the degeneracy of the modes (the $2l+1$ singlets get different frequencies), an effect known as splitting.

The splitting of a given mode can be described in terms of a splitting function [e.g. *Woodhouse and Giardini*, 1985], which represents the radially averaged structure as seen by the mode. Using perturbation theory, the splitting function coefficients c_{st} are related linearly to the perturbations of the reference Earth model by

$$c_{st} = \int_0^a \delta m_{st}\,(r)\, K_s\,(r)\,\mathrm{d}r + \sum_d \delta h_{st}^d H_s^d \tag{1}$$

where m_{st} represents various model parameters (e.g. seismic velocities, density, anisotropy), d represents the internal discontinuities with undulation δh_{st}, both expanded in spherical harmonics of angular order s and azimuthal order t, and $K_s\,(r)$, H_s^d are the associated sensitivity kernels [*Woodhouse*, 1980]. Splitting function maps $F(\theta,\phi)$ are used to visualise the splitting function coefficients:

$$F(\theta,\phi) = \sum_{s=0}^{2l} \sum_{t=-s}^{s} c_{st} Y_s^t(\theta,\phi) \tag{2}$$

where $Y_s^t\,(\theta,\phi)$ are the complex spherical harmonics of *Edmonds* [1960]. The values of the splitting function $F(\theta,\phi)$ can be interpreted as the local radially averaged deviation from the degenerate frequency of the multiplet.

In recent years, the quantity and quality of normal-mode data have improved substantially, due to the occurrence of several megathrust earthquakes such as the Sumatra events of 2004 (Mw=9.0) and 2005 (Mw=8.6) and the 2010 Chile event (Mw=8.8). We adopt the dataset of splitting functions of normal modes obtained by *Deuss et al.* [2012] after inversion of normal mode spectra from 91 large earthquakes in the time range 1976-2010. For the inversion of spectra, synthetic seismograms $u(t)$ are computed by summation of

normal modes using the method of *Deuss and Woodhouse* [2001] and can be written as a harmonic function of time t:

$$u(t) = \Re e \left[\mathbf{r} \cdot \exp^{i\sqrt{\mathrm{M}}t} \cdot \mathbf{s} \right] \tag{3}$$

where $\mathbf{r}$ and $\mathbf{s}$ are the source and receiver vector respectively and M is the matrix containing all the splitting function coefficients. Observed normal mode spectra are then fitted in an iterative way to obtain the optimum splitting function coefficients. Since our focus is to distinguish the effect of different CMB topography maps on the normal modes, we only consider modes whose sensitivity kernels are most sensitive to CMB undulations, as demonstrated by *Koelemeijer et al.* [2012]. This results in a set of 16 normal modes from this data set with radial order $n = 0 - 5$ for which the sensitivity kernels are given in Figure 2.

We firstly compute synthetic splitting functions associated with mantle heterogeneity (no CMB topography), based on 3D mantle model S20RTS [*Ritsema et al.*, 1999], using crustal model Crust5.1 [*Mooney et al.*, 1998] to correct for crustal thickness, surface topography and sea level. P-wave velocity and density heterogeneities are scaled to S-wave velocity using $\delta \ln V_p / \delta \ln V_s$=0.5 and $\delta \ln \rho / \delta \ln V_s$=0.3, consistent with previous work [*Karato*, 1993; *Li et al.*, 1991a]. The observed splitting functions were already corrected for rotation and ellipticity, hence no correction is needed for the synthetic splitting functions.

Using a scaled S-model to account for P heterogeneity is preferable to using independent S and P models because: (i) modes are much more sensitive to S than P velocity; (ii) global S models are generally better resolved and more reliable than corresponding P models; (iii) implementation is simpler (no need to re-parameterize a P model). In addition, *Soldati et al.* [2012] show in their Figures 8, 9 and 14 that P-velocity mantle models associated to

all the CMB models presented here differ only slightly: differences in the data-fit found here can thus be ascribed to the important differences in CMB topography.

We subsequently compute the splitting due to heterogeneous CMB topography, based on the CMB topography models obtained by *Soldati et al.* [2012] applying alternatively a classic tomography approach (T) [e.g. *Morelli and Dziewonski*, 1987; *Boschi and Dziewonski*, 2000] and the joint tomography-geodynamic (TG) approach summarised in Section 1 (Figure 1). The geodynamic 'regularisation' is based on different rheology profiles. Model *cmbTG* is based on the radial viscosity profile proposed by *Mitrovica and Forte* [1997]. Models $cmbTG_{ppv200}$ and $cmbTG_{ppv250}$ are derived using a modified profile that accounts for a post-perovskite layer via a reduction of viscosity of three orders of magnitude [*Cizkova et al.*, 2010] in the lowermost 200 km and 250 km of the mantle respectively.

3. Results

In Figure 3 we present the splitting coefficients predictions for the c_{20} and $\mathrm{Im}(c_{22})$ coefficients associated with the 16 modes used in this study. Instead of plotting the actual value of the prediction, we plot the difference from the S20RTS+Crust5.1 prediction to be able to see the variations. We choose to show these coefficients as they are important contributors to the Pacific 'Ring-of-fire' pattern observed in lowermost mantle tomography models. Values close to zero indicate small variations from S20RTS+Crust5.1. The data are fitted better by the CMB topography maps than S20RTS+Crust5.1 when the predictions plot on the same side of the horizontal line as the data.

For some modes, the predictions with added CMB topography move towards the observed splitting coefficients as is the case for the fundamental modes ${}_0S_4$-${}_0S_9$ ($\mathrm{Im}(c_{22})$ coefficient) and the first order overtones ${}_1S_8$-${}_1S_{10}$ and ${}_1S_{14}$ (c_{20} coefficient). However, in

other cases, such as for the third order overtones ${}_3S_8$-${}_3S_9$ (both coefficients) the predictions for CMB topography move away from the data. Generally, these trends depend on the mode and coefficient in question. For some modes, we have observations up to structural degree $t = 12$, hence a total number of 80 coefficients. Therefore, looking at individual coefficients does not give a straightforward way of determining the best CMB topography map. In addition, *Koelemeijer et al.* [2012] demonstrated that the splitting functions can be also influenced by other structures, such as anisotropy and ultra low velocity zones, which are not accounted for here.

We calculate misfit values between the observed splitting functions and the predictions for the different CMB topography maps to quantitatively assess the best CMB topography map. To this purpose, we define the L^1 and L^2 norms for structural degree s as

$$L_s^a = \frac{1}{16} \sum_{modes} \frac{1}{2s+1} \sum_{t=-s}^{s} \left| c_{st}^{model} - c_{st}^{data} \right|^a \tag{4}$$

where c_{st}^{model} are the predicted splitting function coefficients for the CMB topography maps on top of S20RTS+Crust5.1 using Equation 1 and c_{st}^{data} are the coefficients of the observed splitting functions. a is either 1 or 2 for the L^1 and L^2 norms respectively. In this definition, the misfit is not normalised as otherwise small coefficients (which contain little information about structure) dominate the misfit. We also normalise the misfit by the associated uncertainties σ_{st}^{data} in the data to give more weight to coefficients with small measurement uncertainties. These uncertainties were estimated using the maximum range in observed coefficients in 10 cross-validation runs, with different events being left out in different runs [*Deuss et al.*, 2012].

The misfit to the data is summarised in Table 1 for different structural degrees and all degrees for which we have data (up to $s = 12$) together. Degree 2 misfits have the highest

absolute values as these coefficients have the largest amplitude in the data. Except at degree 6, the misfit values for all geodynamically-constrained tomography maps are lower than the misfits for the pure seismic one. On top of that, the misfit values for $cmbTG_{ppv200}$ and $cmbTG_{ppv250}$ are very similar but always lower than the values for $cmbTG$. This suggests that the addition of a low viscosity post-perovskite layer fits the observations better, although the thickness of the layer is less important. For degree 2 and 4, the $cmbTG_{ppv250}$ produces the smallest misfit out of the different CMB topography maps whereas for degree 6 the $cmbTG_{ppv200}$ has a lower misfit.

The same test conducted on the basis of tomographic model S40RTS [*Ritsema et al.*, 2011] (derived inverting also the normal mode splitting observations from *Deuss et al.* [2012]) instead of S20RTS obtained better fit to the data but gives analogous conclusions: misfit values are lowest for the $cmbTG_{ppv}$ CMB topography maps for both the L^1 and L^2 norms as demonstrated in Table 2 for all degrees together. This table also gives the misfit values when we use the associated uncertainties to normalise the misfit. In this case, the $cmbTG_{ppv}$ maps perform best except when the L^1 norm is used with S20RTS as basis. However, in this case, the difference with the $cmbTG_{ppv250}$ map is less than a percent and not significant.

In the remainder of this letter we choose to display the not normalized misfit as we found that misfit values using the data or uncertainties as normalization are dominated by few coefficients with anomalous small values.

4. Robustness estimate

Generally, the difference in misfit between the $cmbT$ and $cmbTG_{ppv}$ maps is similar in magnitude to the difference in misfit between the S20RTS and S40RTS predictions.

This indicates that these results are robust; yet, a more quantitative estimate of their significance is necessary.

4.1. Random model test

To test the significance of the misfit values, we generate 1000 random models of CMB topography with the same harmonic spectrum as our preferred maps but with different geographic patterns. Given that the CMB topography maps differ quite significantly in amplitude, we use two different models as our basis for the random models. We use primarily the $cmbTG_{ppv200}$ map which has a low amplitude and gives us a conservative estimate. A larger amplitude map such as for the $cmbTG$ model is expected to give higher confidence numbers as the normal modes favour low amplitude topography maps. We compute the splitting functions for these models and calculate the misfit of these predictions with the data for the same selection of modes. In this way, we're testing how likely it is that we improve the fit 'by chance' rather than physical reasons. For example, if 100 out of 1000 models have a lower misfit than the real model, this indicates that the misfit of the real model is 90 % significant. By restricting ourselves to models with the same amplitude spectrum as the real model, we are also conservative in the sampling of the null space.

Figure 4 shows the histograms of the L^2 norm obtained for degree 2, 4, 6 and all degrees together for random models based on the $cmbTG_{ppv200}$ map. For degree 2 and 4, the $cmbTG_{ppv}$ maps have misfits very close together at a significance level of 92 % and 75 % respectively. However, for degree 6, the CMB topography models generally have a higher misfit than the random models. When all degrees are considered together, the $cmbTG_{ppv200}$ model has the lowest misfit, at a 99.7 % significance level.

The bimodal shape characterising the degree 2 distribution of misfit achieved by the random CMB models may be an effect of the harmonic spectrum, which is strongly dominated by degree 2. Depending on the (random) sign of the $l = 2$, $m = 0$ coefficient, two classes of models emerge: one resembling the real world, with elevated topography under South Africa and the Pacific; the other anti-correlated, and hence inconsistent with the data. This bimodal distribution is also evident in the misfit for all degrees, which is dominated by degree 2. We report in Table 3 the relative number of random CMB topography models based on both the $cmbTG_{ppv200}$ and $cmbTG$ maps which fit the data better than all the different models of mantle/CMB topography employed here. We can see that especially for degree 2 and 4, the reduction in misfit for the $cmbTG_{ppv}$ models is significant. For each degree, the significance numbers based on the two different CMB topography maps agree. Hence we can confidently use the more conservative significance estimates based on model $cmbTG_{ppv200}$.

4.2. Observability

We have used the misfit and the random model test to show that the reduction in misfit is significant. However, we also want to know whether the normal mode data used here are sensitive to the differences between these CMB topography models. To this purpose, we use the concept of observability [*Koelemeijer et al.*, 2012] defined as:

$$O_s = \frac{1}{2s+1} \sum_{t=-s}^{s} \frac{\left| c_{st}^A - c_{st}^B \right|}{\sigma_{st}^{data}} \tag{5}$$

where c_{st}^A and c_{st}^B are the splitting function coefficients for two models A and B and σ_{st}^{data} are the associated uncertainties in the data [*Deuss et al.*, 2012]. The observability provides us with a quantitative measure to assess whether small variations in synthetic splitting functions are significant enough with respect to the data limitations. Observability values

larger than 1 indicate that the difference between two models is larger than the uncertainty in the data and hence it is significant. As a rule of thumb, if more than half of the O_s values are above 1, we would call the difference between those models observable under the current data uncertainties. We calculate the observability of the CMB topography maps with respect to the S20RTS+Crust5.1 predictions and between the different CMB topography maps. In Figure 5 we show the degree 2 observability (O_2) values for the selection of normal modes.

The observability values summed for each mode (Figure 5a) indicate that the CMB topography maps *cmbT* and *cmbTG* are easiest to observe (12 above versus 4 below 1) whereas when a low viscosity layer is added ($cmbTG_{ppv200}$ and $cmbTG_{ppv250}$), the observability is reduced (6 above versus 10 below 1). The same is true when looking at the observability for individual coefficients (Figure 5b-e), where the signal due to the $cmbTG_{ppv}$ models is mainly within the uncertainty of the data (20-30 above versus 60-50 below 1). However, these are observability values with respect to the S20RTS+Crust5.1 predictions whereas we are interested in the observability between different CMB topography models. In that case, the observability values are in fact larger; the difference between the *cmbT* and *cmbTG* maps are close to the data uncertainties (30 above versus 50 below 1) but the difference between the *cmbT* and $cmbTG_{ppv250}$ maps is more observable (40 above versus 40 below 1). This implies that the normal modes are able to observe the difference between these kind of models, although being close to the data uncertainties, and hence that the difference in misfit we observe is significant.

The peak-to-peak amplitude of the CMB topography maps decreases with increasing complexity from 12.4 km for *cmbT*, 8.7 km for *cmbTG*, 3.5 km for $cmbTG_{ppv200}$ to 2.1 km

for $cmbTG_{ppv250}$. One may think that the better fit we obtain for the $cmbTG_{ppv}$ maps is purely due to the amplitude of the topography maps with the normal modes preferring smaller amplitudes. Given that the amplitude of the topography is of more influence than its pattern [*Koelemeijer et al.*, 2012], it is difficult to assess whether this is the case. The random test models show that even when we have the same amplitude spectrum, the misfit of the desired maps are significantly lower than those of the random maps, at least for degree 2 and 4. Additionally, both the $cmbTG_{ppv}$ maps fit the requirement of a peak-to-peak amplitudes less than 5 km, and as a result they are our preferred maps on the basis of all these considerations.

5. Summary

We calculate synthetic splitting functions for different CMB topography maps on top of the 3D mantle S-wave model S20RTS and crustal model Crust5.1. The maps of CMB topography employed (retrieved via purely seismic or geodynamically constrained tomographic inversions of P-wave data) generally fit the normal mode splitting observations. Introducing the geodynamic term in the CMB topography maps, constrained by the mechanical coupling with lowermost mantle structure, helps with respect to pure tomography. Accounting for the presence of post-perovskite in the form of a low viscosity layer at the base of the mantle reduces the misfit further. As the improvements in misfit are small, we assess the significance of these results using a random model test and the concept of observability. The random model test demonstrates that the reduction in misfit of the $cmbTG_{ppv}$ maps is about 92 % significant for degree 2 and about 98 % significant for all degrees together. The observability values indicate that some of the maps are within the uncertainty of the data. However, normal modes are able to observe the differences

between the different CMB topography maps, implying that the reduction in misfit is significant enough. We can thus state that our CMB tomography maps $cmbTG_{ppv}$ significantly improve the fit to the normal mode observations, while at the same time being geodynamically consistent. This implies that joint seismic-geodynamic inversions and the incorporation of a low viscosity layer are important steps towards a more realistic modelling of the Earth's lowermost mantle.

Acknowledgments. We thank Mark Panning and an anonymous reviewer for helpful reviews of this manuscript. AD and PJK are funded by the European Research Council under the European Community's Seventh Framework Programme (FP7/2007-2013)/ERC grant agreement number 204995. AD was supported by a Philip Leverhulme Prize and PJK was also supported by the Nahum Scholarship in Physics and a Graduate Studentship, both from Pembroke College, Cambridge. Figures have been produced using the GMT software [*Wessel and Smith*, 1998].

References

Ammann, M. W., J. P. Brodholt, J. Wookey, and D. P. Dobson (2010), First-principles constraints on diffusion in lower-mantle minerals and a weak D " layer, *Nature*, *465*(7297), 462–465.

Benioff, H., F. Press, and S. Smith (1961), Excitation of the free oscillations of the Earth by earthquakes, *Journal of Geophysical Research*, *66*(2), 605–619.

Boschi, L., and A. M. Dziewonski (2000), Whole Earth tomography from delay times of P, PcP, and PKP phases: Lateral heterogeneities in the outer core or radial anisotropy in the mantle?, *J. Geophys. Res.*, *105*(B6), 13,675–13,696.

Cizkova, H., O. Cadek, C. Matyska, and D. A. Yuen (2010), Implications of post-perovskite transport properties for core-mantle dynamics, *Phys. Earth Planet. Inter.*, *180*(3-4), 235–243.

Deuss, A., and J. Woodhouse (2001), Theoretical free-oscillation spectra: the importance of wide band coupling, *Geophys. J. Int.*, *146*(3), 833–842.

Deuss, A., J. Ritsema, and H. Van Heijst (2012), A new catalogue of normal-mode splitting function measurements up to 10 mHz, *Geophys. J. Int.*, *submitted*.

Edmonds, A. (1960), *Angular momentum in quantum mechanics*, Princeton University Press.

Forte, A. M., J. X. Mitrovica, and R. L. Woodward (1995), Seismic-geodynamic determination of the origin of excess ellipticity of the core-mantle boundary, *Geophys. Res. Lett.*, *22*(9), 1013–1016.

Gwinn, C. R., T. A. Herring, and I. I. Shapiro (1986), Geodesy by radio interferometry - studies of the forced nutations of the earth .2. interpretation, *J. Geophys. Res-solid. Earth. Pl.*, *91*(B5), 4755–4765.

Ishii, M., and J. Tromp (1999), Normal-mode and free-air gravity constraints on lateral variations in velocity and density of Earth's mantle, *Science*, *285*(5431), 1231–1236.

Karato, S.-I. (1993), Importance of anelasticity in the interpretation of seismic tomography, *Geophys. Res. Lett.*, *20*, 1623–1626.

Koelemeijer, P., A. Deuss, and J. Trampert (2012), Normal mode sensitivity to Earth's D" layer and topography on the core-mantle boundary: what we can and cannot see, *Geophys. J. Int.*, *190*(1), 553–568.

Lassak, T. M., A. K. McNamara, and S. Zhong (2007), Influence of thermochemical piles on topography at Earth's core-mantle boundary, *Earth Planet. Sci. Lett.*, *261*(3-4), 443–455.

Lassak, T. M., A. K. McNamara, E. J. Garnero, and S. J. Zhong (2010), Core-mantle boundary topography as a possible constraint on lower mantle chemistry and dynamics, *Earth Planet. Sci. Lett.*, *289*(1-2), 232–241.

Li, X., D. Giardini, and J. Woodhouse (1991a), The relative amplitudes of mantle heterogeneity in P velocity, S velocity and density from free-oscillation data, *Geophys. J. Int.*, *105*(3), 649–657.

Li, X. D., D. Giardini, and J. H. Woodhouse (1991b), Large-scale 3-dimensional even-degree structure of the earth from splitting of long-period normal-modes, *J. Geophys. Res-solid.*, *96*(B1), 551–577.

Mitrovica, J., and A. M. Forte (1997), The radial profile of mantle viscosity: results from the joint inversion of convection and post-glacial rebound observables, *J. Geophys. Res.*, *102*, 2751–2769.

Mooney, W. D., G. Laske, and T. G. Masters (1998), Crust 5.1: A global crustal model at 5 degrees x 5 degrees, *J. Geophys. Res.*, *103*(B1), 727–747.

Morelli, A., and A. M. Dziewonski (1987), Topography of the core-mantle boundary and lateral homogeneity of the liquid core, *Nature*, *325*, 678–683.

Mosca, I., L. Cobden, A. Deuss, J. Ritsema, and J. Trampert (2012), Seismic and mineralogical structures of the lower mantle from probabilistic tomography, *J. Geophys. Res.*, *117*, doi:10.1029/2011JB008851.

Murakami, M., K. Hirose, K. Kawamura, N. Sata, and Y. Ohishi (2004), Post-perovskite phase transition in mgsio3, *Science*, *304*, 855.

Nakagawa, T., and P. J. Tackley (2005), The interaction between the post-perovskite phase change and a thermo-chemical boundary layer near the core-mantle boundary, *Earth Planet. Sci. Lett.*, *238*(1-2), 204–216.

Obayashi, M., and Y. Fukao (1997), P and PcP travel time tomography for the core-mantle boundary, *J. Geophys. Res.*, *102*, 17,825–17,841.

Oganov, A. R., and S. Ono (2004), Theoretical and experimental evidence for a post-perovskite phase of mgsio3 in earth's d" layer, *Nature*, *430*, 445.

Ritsema, J., H. J. V. Heijst, and J. H. Woodhouse (1999), Complex shear wave velocity structure imaged beneath Africa and iceland, *Science*, *286*(5446), 1925–1928.

Ritsema, J., A. Deuss, H. J. van Heijst, and J. H. Woodhouse (2011), S40RTS: a degree-40 shear-velocity model for the mantle from new Rayleigh wave dispersion, teleseismic traveltime and normal-mode splitting function measurements, *Geophys. J. Int.*, *184*(3), 1223–1236.

Rodgers, A., and J. Wahr (1993), Inference of core-mantle boundary topography from isc pcp and pkp traveltimes, *Geophys. J. Int.*, *115*, 991–1011.

Soldati, G., L. Boschi, and A. Piersanti (2003), Outer core density heterogeneity and the discrepancy between PKP and PcP travel time observations, *Geophys. Res. Lett.*, *30*(4), 1190.

Soldati, G., L. Boschi, and A. M. Forte (2012), Tomography of core-mantle boundary and lowermost mantle coupled by geodynamics, *Geophys. J. Int.*, *189*(2), 730–746.

Sze, E., and R. van der Hilst (2003), Core mantle boundary topography from short period PcP, PKP, and PKKP data, *Phys. Earth Planet. Inter.*, , *135*(1), 27–46.

Wessel, P., and W. Smith (1998), New, improved version of the generic mapping tools released, *Eos Trans. AGU*, , *79*, 579–579.

Woodhouse, J. (1980), The coupling and attenuation of nearly resonant multiplets in the Earth's free oscillation spectrum, *Geophys. J. R. Astron. Soc.*, , *61*(2), 261–283.

Woodhouse, J., and D. Giardini (1985), Inversion for the splitting functions of isolated normal mode multiplets, *EOS*, *66*, 301–301.

Yamazaki, D., T. Yoshino, H. Ohfuji, J. I. Ando, and A. Yoneda (2006), Origin of seismic anisotropy in the D ” layer inferred from shear deformation experiments on post-perovskite phase, *Earth Planet. Sci. Lett.*, *252*(3-4), 372–378.

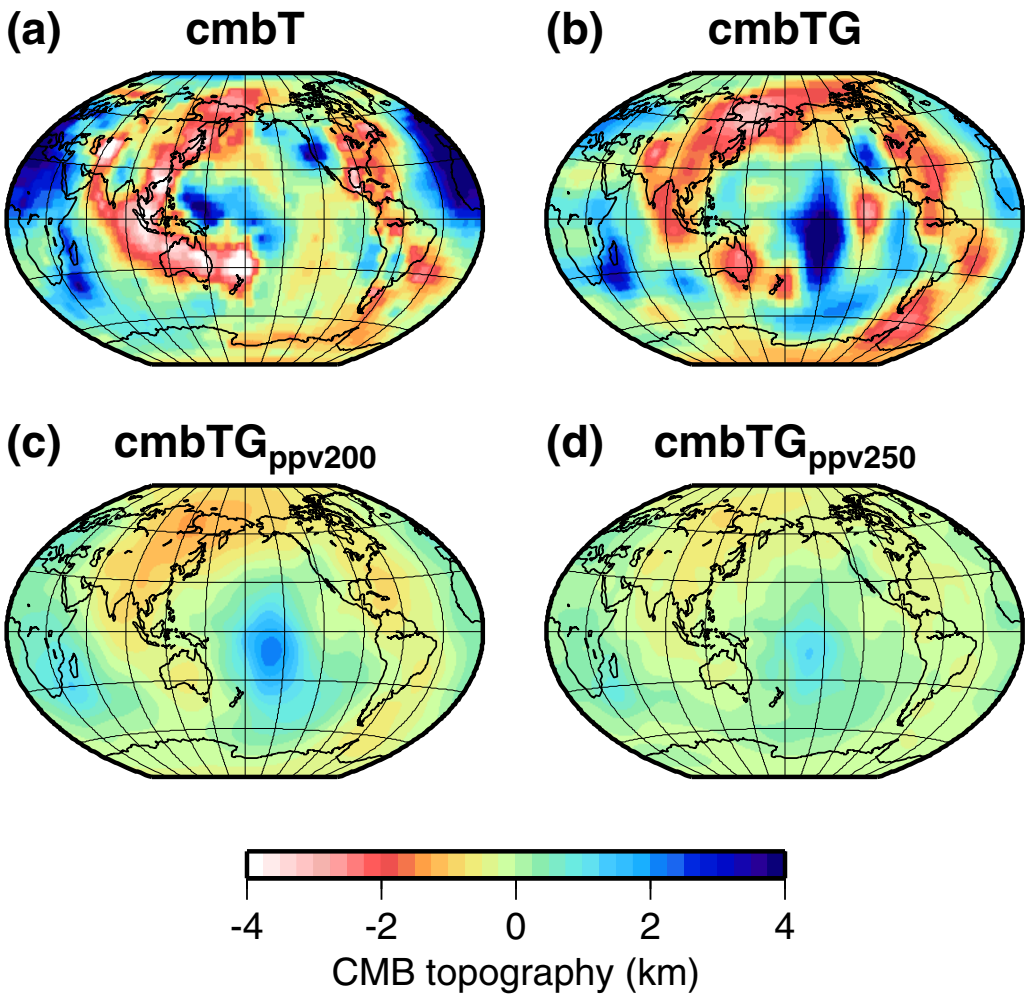

Figure 1. Maps of CMB topography (km) implemented in this study. The maps are derived using (a) a classical tomography approach and (b-d) a joint tomographic-geodynamic approach. A low viscosity post-perovskite layer of varying thickness is included in (c,d).

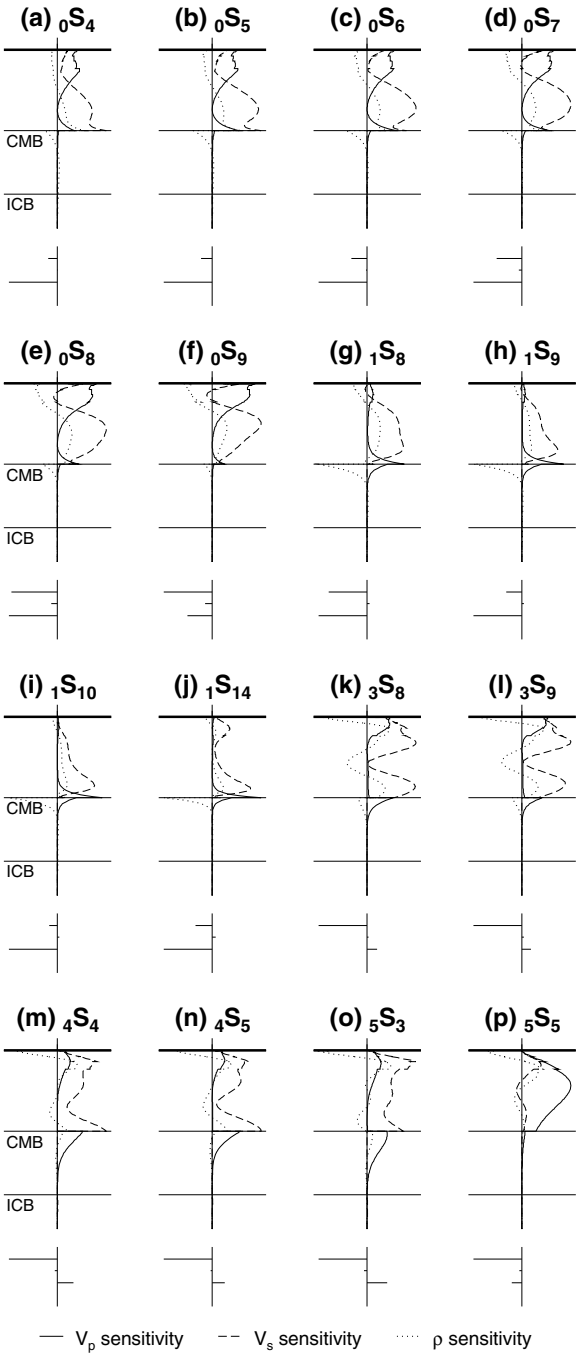

Figure 2. Sensitivity kernels calculated for the set of CMB sensitive modes used in this study showing sensitivity kernels $K_s(r)$ to P-wave velocity (solid), S-wave velocity (dashed) and density (dotted). The radii of the CMB and ICB are indicated by horizontal lines. The horizontal bars underneath the kernels show from top to bottom the mode's sensitivity kernel H_s^d to topographic perturbations of the free surface (blue), the 660-km discontinuity (green), CMB (red) and ICB (black). Each graph is scaled independently.

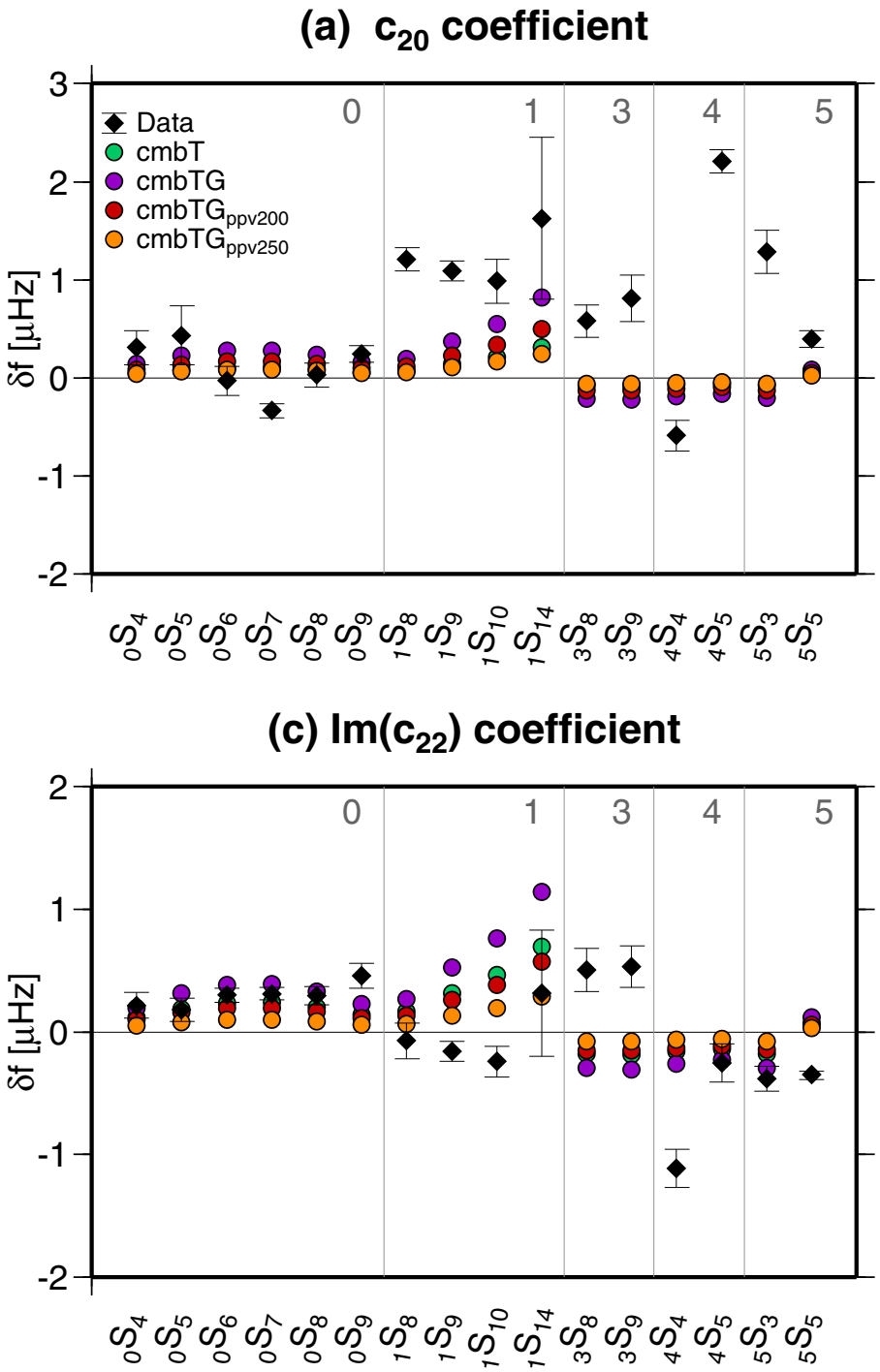

Figure 3. Deviations from the S20RTS+Crust5.1 predictions plotted in μHz for CMB sensitive normal modes (specified along the horizontal axis) for (a) the c_{20} coefficient and (b) the Im(c_{22}) coefficient. The modes are plotted versus angular order l of the mode, separated by vertical lines. Data with error bars (black diamonds) are taken from *Deuss et al.* [2012] and predictions for the CMB topography models of Figure 1 are plotted as coloured circles.

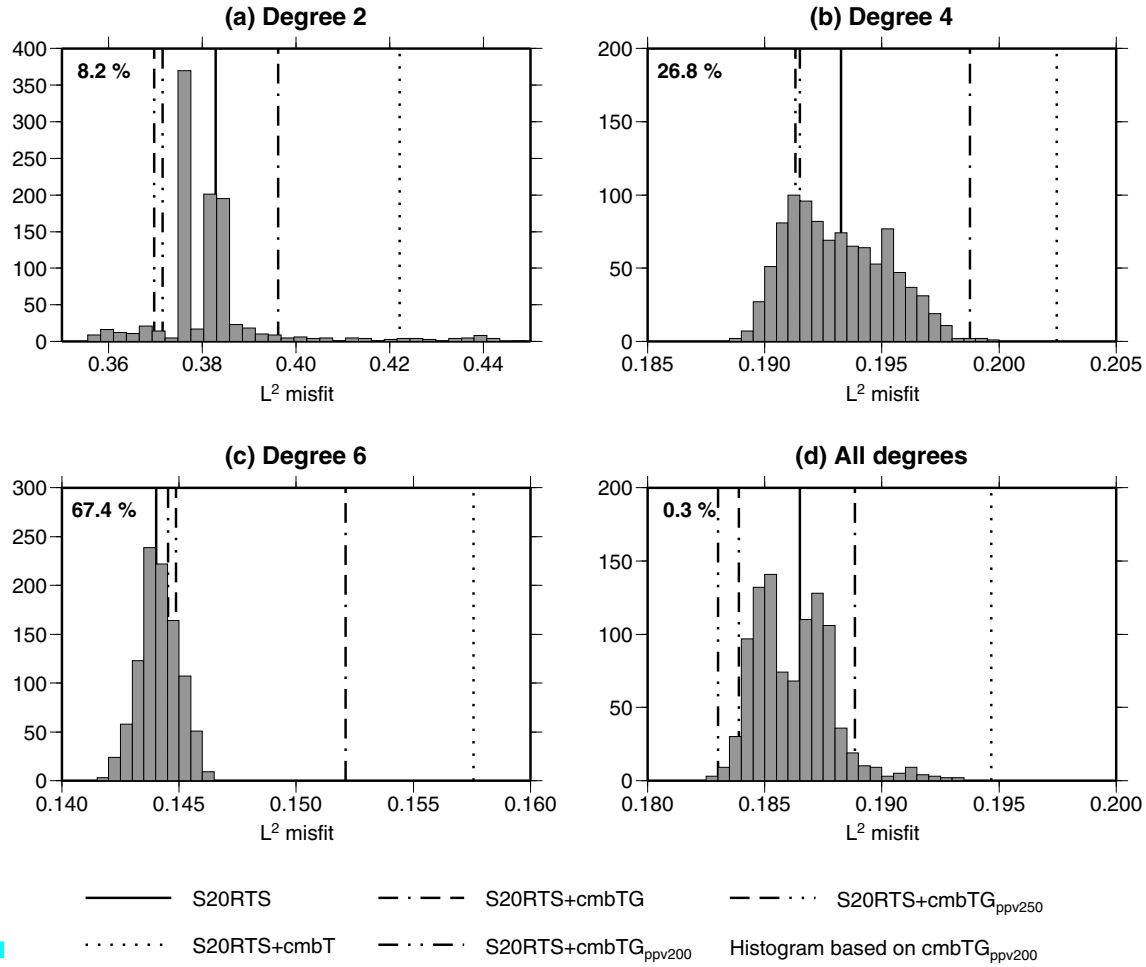

Figure 4. Histograms representing the misfit to the splitting function data achieved by 1000 random CMB models with the same spectrum as model $cmbTG_{ppv200}$ for (a) degree 2, (b) degree 4, (c) degree 6 and (d) all degrees (up to $s = 12$). The misfit values of the topography models themselves are indicated by vertical lines and the percentage represents the number of random models with a lower misfit than $cmbTG_{ppv200}$.

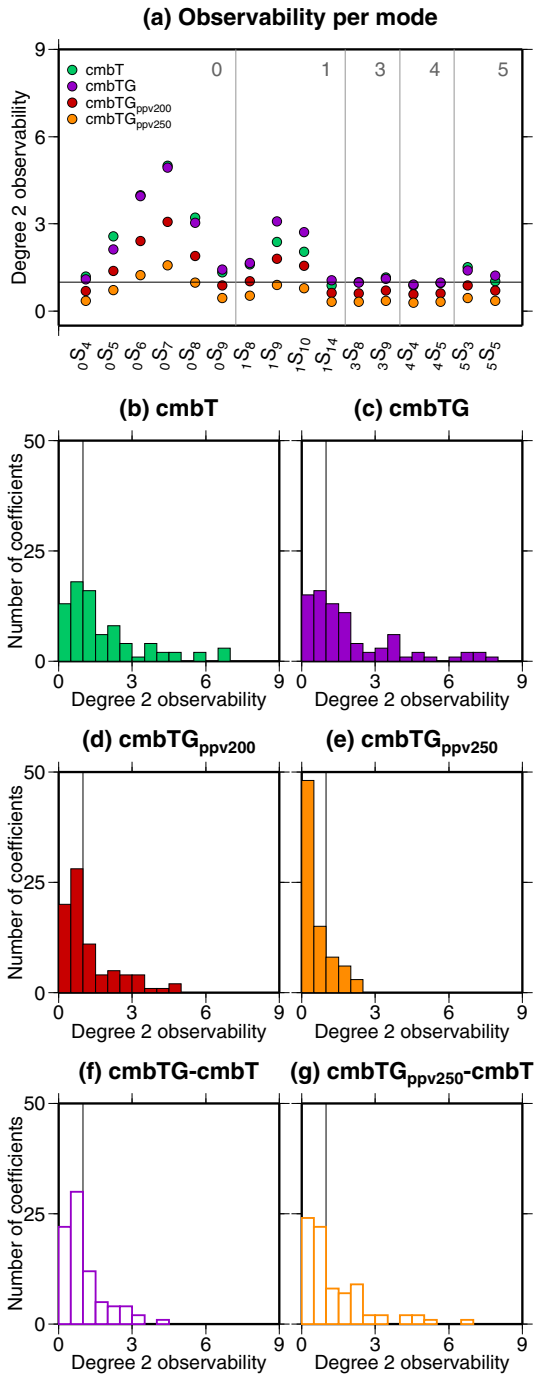

Figure 5. Degree 2 observability values plotted for CMB sensitive modes with in (a) observability values summed for individual modes according to Equation 5. The bottom panels show histograms of degree 2 observability values with respect to the S20RTS+Crust5.1 predictions (b-e) and with respect to the *cmbT* model (f-g) where we have not summed over the coefficients. Values larger than 1 are significant as the signal in the splitting function is larger than the data uncertainty.

Mantle/CMB model	Degree 2	Degree 4	Degree 6	All degrees
S20RTS	0.383	0.193	**0.144**	0.187
S20RTS+*cmbT*	0.422	0.202	0.158	0.195
S20RTS+*cmbTG*	0.396	0.199	0.152	0.189
S20RTS+$cmbTG_{ppv200}$	0.371	0.192	0.145	**0.183**
S20RTS+$cmbTG_{ppv250}$	**0.370**	**0.191**	0.145	0.184

Table 1. Misfit of the synthetic splitting coefficients in μHz based on different CMB topography maps on top of S20RTS+Crust5.1 to the observed splitting function data. The misfit is computed using the L^2 norm (Equation 4) for structural degree 2, 4, 6 and all degrees up to $s = 12$ together. In bold we indicate the lowest misfit value in each case.

	Not normalized [μHz]				Error normalised [-]			
	L^1		L^2		L^1		L^2	
Model	S20RTS	S40RTS	S20RTS	S40RTS	S20RTS	S40RTS	S20RTS	S40RTS
Model	0.292	0.264	0.187	0.164	2.16	1.89	**9.22**	7.25
+*cmbT*	0.301	0.266	0.195	0.163	2.23	1.91	10.2	7.19
+*cmbTG*	0.295	0.261	0.189	0.157	2.22	1.90	10.2	7.21
+$cmbTG_{ppv200}$	**0.289**	**0.260**	**0.183**	**0.155**	2.16	**1.86**	9.42	**6.96**
+$cmbTG_{ppv250}$	0.290	0.261	0.184	0.184	**2.15**	1.87	9.25	7.04

Table 2. Not normalized and uncertainty normalized misfit of the synthetic splitting coefficients for different CMB topography maps on top of S20RTS or S40RTS to the observed splitting function data. The misfit is computed using the L^1 and L^2 norm (Equation 4) for all degrees up to $s = 12$ together. In bold we indicate the lowest misfit value in each case.

Mantle/CMB model	Degree 2	Degree 4	Degree 6	All degrees
S20RTS	60.5 (0)	55.5 (29)	**45.3** (**13**)	45.3 (2)
S20RTS+*cmbT*	96.5 (39)	100 (56)	100 (86)	100 (46)
S20RTS+*cmbTG*	92.9 (0)	99.6 (48)	100 (58)	94.9 (5)
S20RTS+$cmbTG_{ppv200}$	8.2 (0)	26.8 (22)	67.4 (14)	**0.3** (**2**)
S20RTS+$cmbTG_{ppv250}$	**7.3** (**0**)	**21.8** (**21**)	79.7 (15)	3.0 (2)

Table 3. Percentage of random models based on model $cmbTG_{ppv200}$ obtaining a better fit to the data than the model indicated in the first column. Similarly, the value in brackets indicates the number of random models in this case based on model *cmbTG* having a better fit.